---

**Article:**
Edwards, J.M., Danao, L.A. and Howell, R.J. (2013) PIV Measurements and CFD Simulation of the Performance and Flow Physics and of a Small-Scale Vertical Axis Wind Turbine. Wind Energy. Published online 17 Dec 2013. ISSN 1095-4244,

https://doi.org/10.1002/we.1690

---

# PIV Measurements and CFD Simulation of the Performance and Flow Physics and of a Small-Scale Vertical Axis Wind Turbine.

Jonathan M Edwards[1], Louis Angelo Danao[2], Robert J Howell[3]

## Abstract

The aerodynamics generated by a small small-scale vertical axis wind turbine (VAWT) are illustrated in detail as a NACA0022 rotor blade carries out a complete rotation at three tip speed ratios. These aerodynamic details are then linked to the wind turbine performance. This is achieved by using detailed experimental measurements of performance and near blade PIV and also using a 2D RANS based CFD model. Uniquely therefore, the CFD model is validated against both PIV visualisations and performance measurements.

At low tip speed ratios ($\lambda = 2$), the flow field is dominated by large scale stalling behaviour as shown in both the experimental results and simulations. The onset of stall appears to be different between the experiment and simulation, with the simulation showing a gradual separation progressing forwards from the trailing edge, while the experiment shows a more sudden leading edge roll-up. Overall, similar scales of vortices are shed at a similar rate in both. The most significant CFD-PIV differences are observed in predicting flow reattachment. At a higher tip speed ratio ($\lambda = 3$), the flow separates slightly later than in the previous condition and as occurs in the lower tip speed ratio, the main differences between the experiment and the simulation are in the flow reattachment process, specifically that the simulations predicts a delay in the process. At a tip speed ratio of 4, smaller predicted flow separation in the latter stages of the upwind part of the rotation is the main difference in comparison to the experiment.

1. Research Associate, Department of Civil and Structural Engineering, University of Sheffield, Sheffield, United Kingdom. j.m.edwards@sheffield.ac.uk
2. Assistant Professor, Department of Mechanical Engineering, University of the Philippines, Quezon City, Philippines. louisdanao@coe.upd.edu.ph
3. Senior Lecturer in Experimental Aerodynamics, Department of Mechanical Engineering, University of Sheffield, Sheffield, United Kingdom. r.howell@sheffield.ac.uk

# Nomenclature

| | | |
|---|---|---|
| $\mathbf{c}$ | blade chord length | (m) |
| $\mathbf{C_p}$ | power coefficient | |
| $\mathbf{C_{p\text{-}blade}}$ | power coefficient, blades only | |
| $\mathbf{C_{p\text{-}max}}$ | maximum power coefficient | |
| $\mathbf{L}$ | blade length | (m) |
| $\mathbf{N}$ | number of blades | |
| $\mathbf{R}$ | rotor radius | (m) |
| $\mathbf{T}$ | net rotor torque | (Nm) |
| $\mathbf{T_B}$ | blade torque | (Nm) |
| $\mathbf{T_{res}}$ | resistive torque | (Nm) |
| $\mathbf{V_B}$ | blade velocity | (m/s) |
| $\mathbf{V_\infty}$ | blade velocity | (m/s) |
| $\boldsymbol{\alpha}$ | angle of attack | rads or deg |
| $\boldsymbol{\alpha_c}$ | local corrected angle of attack | rads or deg |
| $\boldsymbol{\lambda}$ | tip speed ratio | |
| $\boldsymbol{\psi}$ | azimuth position | rads or deg |
| $\boldsymbol{\sigma}$ | rotor solidity | |
| $\boldsymbol{\omega}$ | rotational speed | rads/s or RPM |

# 1 Introduction

In recent years, interest in the VAWT design has been boosted by an increasing desire for the integration of wind energy into the built environment, where the VAWT presents several potential advantages over the more common HAWT (horizontal axis wind turbine): the VAWT avoids the requirement for yaw (turn to face the wind), may have lower sound emission (due lower tip speed ratio operation, [1]), and shows increased performance in skewed flow [2] - a likely flow scenario over a roof-top. However, while the HAWT is highly developed and is currently used for all large-scale wind farms and numerous small-scale applications in rural locations, the VAWT concept is considerably less-developed.

Simple consideration of the vectors of the blade velocity due to rotation, $\mathbf{V_B}$ ($=\mathbf{R\omega}$) and the freestream velocity, $\mathbf{V_\infty}$, yield a skewed-sinusoidal variation of the angle of attack, $\boldsymbol{\alpha}$, with

changing azimuthal position, $\psi$. The tip speed ratio, $\lambda$ ($=\mathbf{V_B} / \mathbf{V}_\infty$), dictates the range in $\alpha$ experienced by the VAWT blade. At a given $\lambda$, the overall performance is the time-averaged result of the continuously varying aerodynamic forces on the rotor blade within a rotation. Previous work by the authors [3] has shown that the actual local $\alpha$ variation is affected by the rotor impedance, which increases with tip speed ratio and with increased energy extraction (higher power coefficient, $\mathbf{C_p}$). Blades in the downstream region also operate in the wake of the upstream blade passes and the wake of the central drive shaft. Understanding the operation of a VAWT blade is a very complex problem which requires detailed inspection of the flow physics. CFD is well-placed to aid the understanding of the VAWT flow physics; however, the current state of model development is not sufficient to replace experiments [4], [5], [6], [7].

Much of the knowledge of the stalling process on VAWTs has been developed from lift and drag polars obtained from pitching aerofoil studies and simulations, Lee [8], [9], [10] and [11]. This is due to the difficulty of carrying out complex experiments on a rotating turbine. While aerofoil studies have increased the understanding of stalling behaviour, they are still limited in their application because they do not reproduce the same flow conditions as found on VAWTs (lack of wake-wake and wake-support interaction, and a lack of flow induction).

The only other directly relevant studies are due to [12], [13] who also conducted PIV experiments. Fujisawa and Shiubya [13] conducted experiments at extremely low Reynolds numbers but described the successive shedding of two pairs of stall vortices from the blade. The mechanism of dynamic stall was shown to be due to the successive generation of a separation on the inner surface of the blade followed by the formation of roll-up vortices from the outer surface. The work by [12] was on a larger VAWT at Re = $5 \times 10^5$ and $7 \times 10^5$ and $\lambda$ = 2, 3, and 4. Although the convection of the shed vortices away from the blade was not shown, the roll up and magnitude of the vortices was clearly shown to be effected by $\lambda$, with large separations shown at $\lambda$=3 and $\lambda$=2. The flow remained almost completely attached for the $\lambda$=4 case. Both [12] and [13] showed no corresponding performance measurements so relation of the dynamic stalling behaviour to performance could not be made.

It is interesting to note that while the fundamentals of the stalling behaviour is not yet fully understood, some researchers have gone on to develop control methods for the stalling process, using either synthetic jets [14], or plasma actuators [15] which do show improvements in turbine performance.

It remains a fact that, to date, there is simply very little information about the stalling processes on VAWTs that comes with experimental validation from which the modelling accuracy can be assessed. This study aims to tackle these pertinent issues. In the following sections, the development of the CFD model is detailed, as well as the experimental methodologies. Following this, the aerodynamic and performance measurements are validated against both experimental PIV visualisations and performance measurements, which importantly allow the quality of the performance prediction to be assessed with respect to the simulated flow physics.

# 2 Methods

## 2.1 Performance Measurements

### 2.1.1 Wind Tunnel Facility

All experimental testing was conducted using The University of Sheffield, Department of Mechanical Engineering's Low-Speed Wind Tunnel (commissioned in 2011) which is an open circuit suction tunnel with the flow driven by an axial fan located at the outlet. The working section is 1.2m wide, 1.2m high and 3m long. The inlet has a two-dimensional contraction with a ratio of 6.25:1, resulting in a maximum test section velocity of 25m/s and a turbulence intensity of 0.3% or below over the working region. For these experiments a turbulence grid was placed at the start of the working section which raised the turbulence intensity at the turbine to 1%, with approximately 0.01m maximum length scale. This turbulence intensity was chosen because it allows the turbine to generate both positive performance at high TSR as well as very well defined vortices and stalling behaviour at low TSR. Too low turbulence intensity (0.3%) causes negative performance (CP) all throughout the range of TSR tested, whereas higher turbulence intensity (2.6%) suppressed the formation of a leading edge separation bubble that would eventually form into the dynamic stall vortex.

### 2.1.2 Turbine Model

The straight-bladed VAWT rotor (Figure 1) features three NACA0022-profiled blades each having a chord length, **c**, of 40mm, and a blade length, **L**, of 600mm, giving a blade aspect ratio of 15. Each blade was mounted on two low-drag support arms at the 1/4 and 3/4 blade span positions at a radius, **R**=0.35m, leading to a solidity, **σ**, of 0.34 based on the conventional definition (**$\sigma = Nc/R$**). An optical encoder monitored the rotational speed of the rotor, which was also fitted with a Magtrol hysteresis brake to provide a known braking torque when required. The frontal swept area blockage of the turbine is 29%; the literature

has conflicting suggestions of whether this is significant or not in terms of $\mathbf{C_p}$ measurement [12], [17], [18]. The wind tunnel model is intended to address fundamental understanding of VAWT performance, and the $\mathbf{C_p}$ stated is not intended to represent any particular full-scale free-operating device. Absolute levels of performance were not important; only relative values of performance were needed as the paper's aim is to elucidate the flow physics present for comparison to an identical computational model.

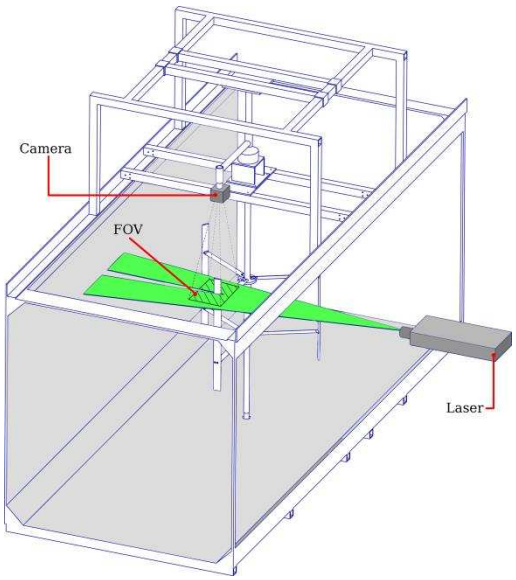


Figure 1. Wind tunnel arrangement showing the VAWT and PIV system.

The measurement equipment designed by the authors to measure torque was calibrated giving a maximum error ±0.01Nm and corresponds to a maximum error of ±5% in the maximum Cp value determined for tests at 7m/s. The error in measurement of turbine rotational speed was negligible. The pressure difference measured by the Pitot-static probe (and a Furness Controls Micromanometer model FC0510) gave an accuracy of the wind speed measurement estimated at 1.25%. The combined potential maximum error in the Cp measurement is therefore ±7.25%. It should be noted that this is exceptionally accurate for a system of this scale.

### 2.1.3 Power Curve Measurement

When testing small wind turbine models, a number of practical problems may be encountered that would perhaps not occur in a 'real-world' device: to obtain a desired Reynolds number, a small VAWT rotates at high speed resulting in large centrifugal forces relative to the turbine

size. The apparatus, being required to withstand such loading, may give system resistances which prevent the turbine from 'cutting-in'. Typically, a VAWT will have a band of $\lambda$ for which positive net torque, **T**, occurs. Outside of this band, **T** will be negative and a small turbine must be driven in order to maintain rotation. Only parts of the **T**- $\lambda$ curve with negative gradient can be measured without a control system to sense rotational speed and adjust opposing torque accordingly [17], [19].

The turbine performance is first measured by allowing the rotor to spin down from a high rotational speed and the deceleration rate monitored using the optical encoder attached to the hysteresis brake. To fully determine the performance of the rotor blades, two spin down tests are required for each test condition. The first involves the spin down of the rotor system without the rotor blades but including the support arms. This is necessary to determine the system resistance (the drag induced by the support arms, as well as resistance of the bearings and hysteresis brake etc). It has been determined that the system resistance is independent of wind speed over the range tested here, i.e. the resistive torque curves from different spin down tests conducted at different wind speeds are identical [3]. The second spin down test is conducted with the rotor blades fitted and so measures the full turbine performance. For both spin down tests, the instantaneous torque is computed by multiplying the instantaneous rotational deceleration ($\xi$) by the turbine's rotational moment of inertia ($I_{rig}$). The rotor blade torque is then the difference between the rotor torque ($\mathbf{T_B}$) and the system resistance ($\mathbf{T_{res}}$), see Equation 1. Instantaneous blade power is derived via Eq. 2. This system is used to determine the performance of the VAWT when it cannot self-sustain itself, i.e. the system resistance (due to bearing friction, and support arm drag) is greater than the torque developed by the rotor blades.

$$T_B + T_{res} + T_{app} = I_{rig}\xi \qquad \text{(Eq. 1)}$$

$$P_B = T_B\Omega \qquad \text{(Eq. 2)}$$

Usefully, this method allows $\mathbf{T_B}$ to be measured so that the rotor blade performance alone can be evaluated, see Equation 2 which allows a direct comparison to be made to the 2D CFD where only the blades are simulated. A detailed assessment of the method can be found in [3].

## 2.2 PIV Measurements

The flow in the wind tunnel was seeded at the inlet with olive oil droplets approximately 2μm in diameter which were generated by a TSI six-jet atomiser. The light sheet was generated by

a Litron Nano L 65-15 Nd:YAG laser (65mJ/pulse) located outside of the tunnel (Figure 1) on an adjustable height platform. A CCD camera of 1600 x 1600 pixels was used together with a narrowband greenpass filter to cut-out interference from other sources of light. To minimise laser light reflection, the blade surface was treated with a Rhodamine 6G-based paint (produced by the authors). To avoid the support arm obscuring a portion of the field of view (FOV), the laser sheet was positioned approximately 3**c** away from the blade tip, and 1.5**c** away from the support arm. It was confirmed through tests at various positions along the span that this position was a good representation of the flow along the majority of the blade length, [19]. For each test, the blade was centered in the reference FOV which was approximately 140mm x 140mm and the integration area used was 32 x 32 pixels, or 2.8mm x 2.8mm. The time interval between exposures was set to yield an approximately eight pixel displacement assuming $\mathbf{V} = 4\,\mathbf{V}_\infty$ based on similar tests carried out by Ferreira et al [12]. 100 ensembles were acquired for each condition tested. The measurements concentrated on three tip speed ratios which were chosen to cover the important and distinct regions of the $\mathbf{C_{p\text{-}blade}}$-$\boldsymbol{\lambda}$ curve (Figure 20, discussed later in Section 3.2):

1) $\boldsymbol{\lambda} = 2$ is near the minimum $\mathbf{C_{p\text{-}blade}}$,
2) $\boldsymbol{\lambda} = 3$ is on the part of the curve where the $\mathbf{C_{p\text{-}blade}}$ is rapidly increasing,
3) $\boldsymbol{\lambda} = 4$ is near the maximum $\mathbf{C_{p\text{-}blade}}$.

Measurements were taken at 10° intervals in $\boldsymbol{\psi}$, following one of the rotor blades, for the first time, through an entire rotation, as illustrated in Figure 2.

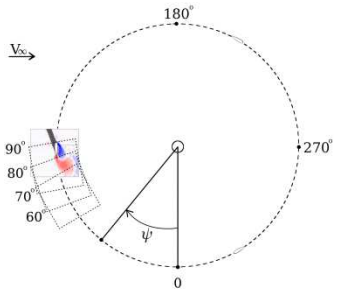


Figure 2. PIV results at different $\psi$ positions showing the rotor blade and FOV.

## 2.3 CFD Model

The commercial CFD code Ansys Fluent 12.1 was used for all of the simulations detailed in this study. The Ansys Fluent 12.1 documentation [21] provides details concerning the governing equations and solver formulation which are not repeated here. Unless stated

otherwise, the recommended values were used for solver settings and model coefficients. The pressure-based solver was used with absolute velocity and second order implicit transient formulation. The coupled pressure-velocity scheme was used, and a second order upwind discretisation was used for all solution variables.

### 2.3.1 Mesh

Earlier studies [4], [19], [22] have shown that the main flow characteristics of the VAWT can be represented using a two-dimensional CFD model. Such a model is unable to account for the effects of the support arms or the blade tip losses on performance; however, this study is concerned with the dominant flow physics of the VAWT, those are secondary effects. The computation time for a three-dimensional simulation would be excessive for a study of this detail.

The model domain consisted of two mesh zones: an inner rotor zone and an outer zone (Figure 3). The mesh of the inner rotor zone rotates together with the blades and the central shaft. The outer domain is fixed and has a rectangular outer boundary (representing the wind tunnel) and a hole in the centre which accommodates the inner rotor zone. At each time step, the solution is interpolated across the sliding interface boundary. The geometry represented a mid-blade slice of the wind tunnel rotor. The simulation of a simple 2D-slice of the wind tunnel set-up would result in a significant over-estimation of blockage. A closer blockage approximation was achieved by matching the ratio of the rotor and wind tunnel widths in the CFD model to that of the rotor and wind tunnel cross-sectional areas in the experiment.

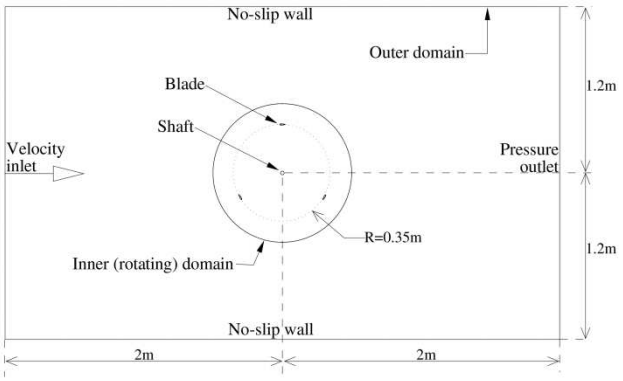


Figure 3. Construction of the overall two-dimensional computational domain.

A wider refinement of the wake region is necessary to resolve important flow structures, which arise due to the wide range in **α.** This was most easily accomplished using a structured O-type mesh which was constructed around each blade (Figure 4) and extended outward

towards the inner zone boundaries (Figure 5). The outer domain was meshed with a simple structured mesh (Figure 6).

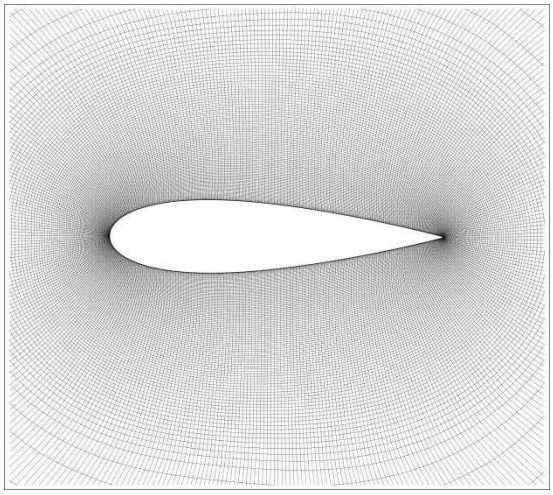

Figure 4. The blade ‘O’ type mesh.

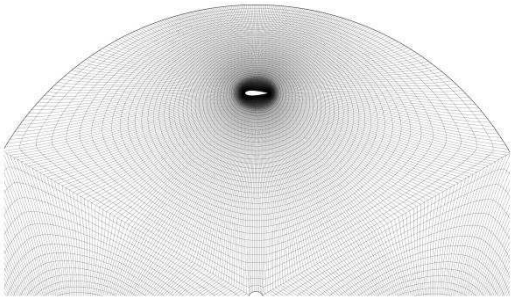

Figure 5. One third of the inner rotor mesh.

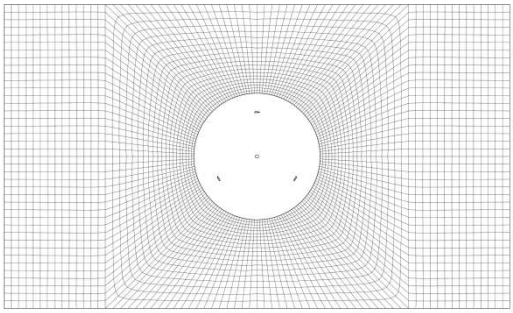

Figure 6. Outer domain mesh.

A mesh sensitivity study was conducted to establish the appropriate node density on the blade surface. Clustering of grid points on the leading edge and trailing edge regions was implemented to provide enough spatial resolution on these key areas. Wall normal spatial resolution was fixed starting with a first cell height small enough to result in acceptable y+ levels between 1 to 5 and all solutions were found to have a y+ of below 2.2 [21]. Growth rate of the inflated boundary layer on the blade surface was fixed to 1.05 and was determined

to be fine enough to provide the required number of layers for boundary layer modelling. Beyond the near-blade mesh, maximum cell edge length within the central region bounded by the blade path was studied. It was concluded that the maximum edge length should be limited to less than half the blade chord to minimise unnecessary dissipation of wake and turbulence generated by the upwind pass of the blades. Blade torque was monitored for the sensitivity study. It was found that 400 points around each blade provided the required node density for accuracy without compromising computational time. A difference of less than 1% in instantaneous blade torque all around a rotation as can be seen in Figure 7.

.

### 2.3.2 Turbulence Model Selection

The turbulence model selection was initially carried out by attempting to match flowfield visualisations and force measurements of a pitching aerofoil study, conducted by [22]. The range in $\boldsymbol{\alpha}$ tested results in the aerofoil undergoing dynamic stall and reattachment, which is also characteristic of the VAWT and the study therefore represents a simplified test case. It will be shown later that the excellent matching of the flow physics between the experiment and the simulations vindicates this approach. Obtaining force data (lift and drag) from a small VAWT rotor blade is extremely difficult and subject to significant errors [16] so data sets from pitching aerofoil studies are a useful source for validation. The lift and drag predictions of the three most suitable models are shown in Figures 7 and 8. Other models were tested (standard k-ε, k-ω, and a laminar solution) but the quality of prediction was found to be poor and so, for brevity, the results are not presented here.

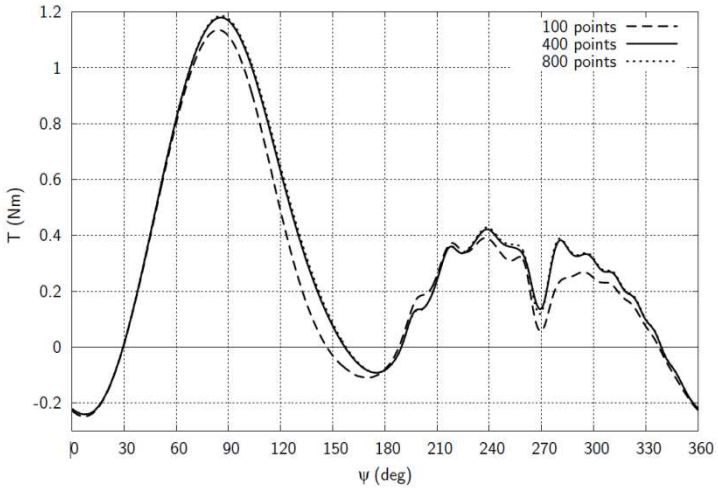


Figure 7. Effect of nodal density around the blade on torque generated.

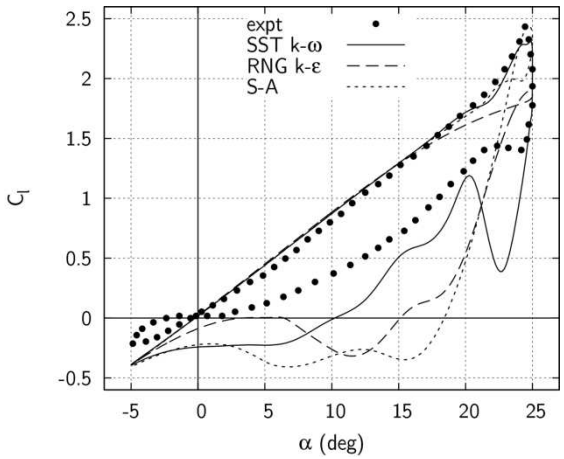


Figure 8. Lift coefficient results for the turbulence model selection process shown compared to measurements of a pitching aerofoil study from [8]

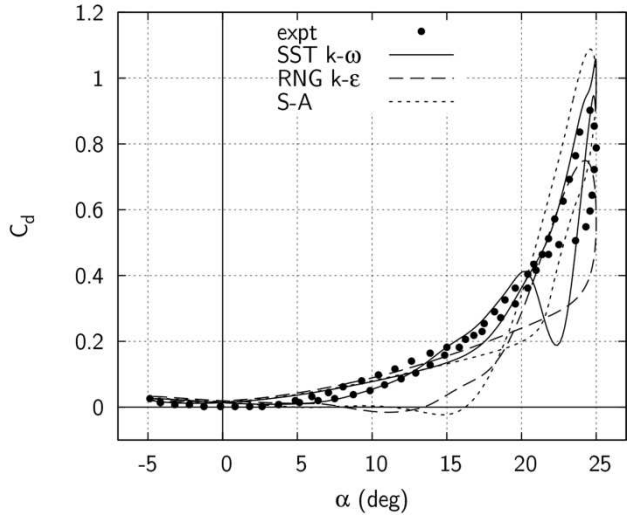


Figure 9. Drag coefficient results for the turbulence model selection process shown compared to measurements of a pitching aerofoil study from [8]

The results of the study showed that the SST k-ω model gave a the best prediction for the region of enhanced lift (Figure 8) which occurs due to the roll-up of the leading edge vortex which is then convected over the aerofoil surface. The early post-stall lift behaviour was also well-matched for the initial drop in lift occurring as the vortex begins to leave the surface. While the region of reduced lift and delayed reattachment was over-predicted by all of the models, the SST k-ω model was again the closest to the experimental data. Drag prediction was also well-matched for the increasing region of the pitching motion (Figure 9). Again, all of the models struggled to accurately simulate the curve hysteresis, with the SST k-ω model giving the closest match, particularly in the $\boldsymbol{\alpha}$ = 15° to -5° region. It is interesting to note that in the predictions of the VAWT aerodynamics, the SST k-ω model is actually significantly

better performing that in this case indicating that, perhaps, the pitching blade is an even more challenging test case.

Plots of the experimental and simulated vorticity flowfields were compared to further establish the suitability of the SST k-ω model (Figure 10). Vorticity is plotted here and in figures which follow because it is a vector field that describes the local spinning motion of a fluid and is ideal for bringing out details of stalled flow and shear layers.

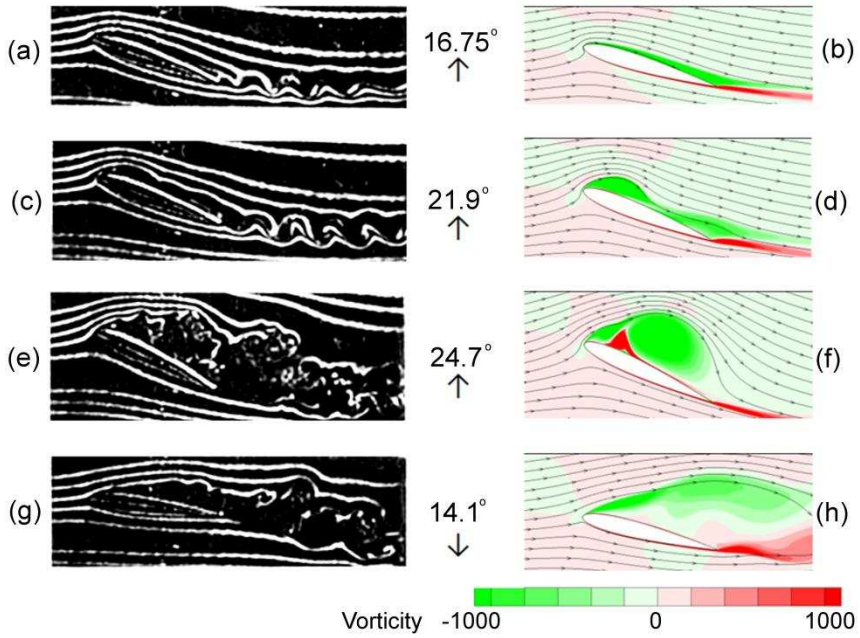


Figure 10. A plot showing the stream lines for different angles of attack from [8]. Simulations are from the SST k-ω model showing contours of vorticity.

The complete cycle of the development and shedding of the dynamic stall vortex was shown to be well-predicted by the model which correctly showed the flow reversal at the trailing edge, and the subsequent formation of a separation bubble at the leading edge which rapidly grew and eventually evolved into the dynamic stall vortex that was convected downstream and finally detached from the aerofoil surface.

Overall, the results of the pitching aerofoil study indicated that the SST k-ω model is the best choice for the prediction of the VAWT blade stalling process and it was chosen for all of the subsequently detailed simulations. This decision is further validated by the closeness with which the CFD predictions match the measurements taken with the PIV system.

### 2.3.3 Time Step and Convergence

The unsteady simulation was stepped forward in time, with up to 50 iterations carried out at each time step to achieve convergence. The chosen size of the time step and the number of iterations were a compromise between solution accuracy and computation time. The rotational position has the most significant influence on the VAWT blade flow physics, and so the solution was stepped forward using a time interval corresponding to a particular azimuthal increment angle. A sensitivity study using simulations with different azithumal angle steps indicated similar torque histories were achieved for time steps which corresponded to $\psi$ increments of less than 2°. A time step corresponding to an azimuthal displacement of 0.5°, at the particular $\lambda$ being simulated, was therefore chosen as the best compromise between solution accuracy and computation time, this value was used for all of the simulations presented in this study. Differences in torque output were less than 1% between time step corresponding to 0.5° and 1°.

The solution was initiated using the inlet velocity value, with a turbulent intensity of 1% and a length scale of 0.01m defined in order to match the wind tunnel case. A large starting vortex resulted from the onset of the rotation of the VAWT and a number of rotations needed to be completed before the initial transients were convected out of the domain.

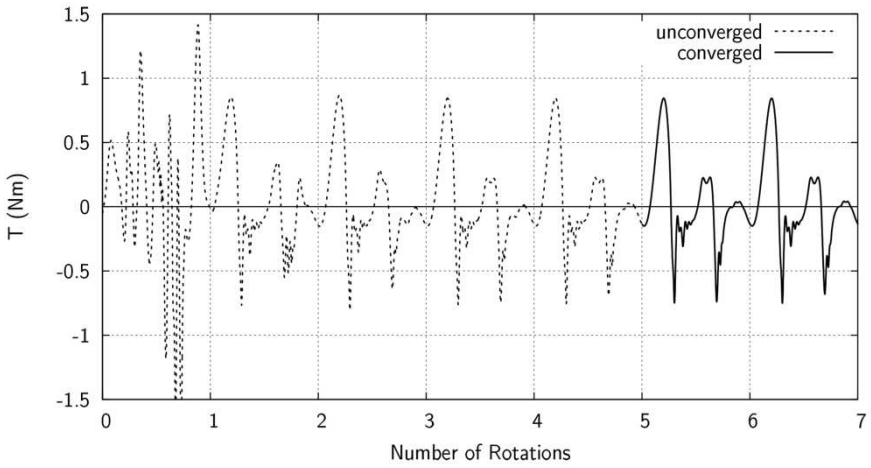


Figure 11. Torque generated with iteration showing periodic convergence.

The torque curve history for a complete solution shows that convergence of the forces occurs in around 5 to 10 rotations depending on $\lambda$, see Figure 11. At higher $\lambda$, a higher number of rotations were completed before periodic convergence was achieved. The solution residuals were also checked to ensure that they were reduced by 6 orders of magnitude at the point at which the torque curve convergence was observed.

The aim of this study is to show what is possible by using a current commercial CFD package which is likely to be available to many current design engineers working on VAWT development. More importantly, this study aims to more fully explain the dynamics of the flow than has been achieved before and this is necessary for the progression of VAWT flow understanding and therefore future development.

# 3 Results

In this section, the results of the CFD simulation with the previously selected turbulence model are compared against both PIV visualisations and performance measurements. It is the aerodynamic physics that dictates the turbine performance so it is vital that the two are understood together. This is the first time this has been carried out in such detail and for a full rotor revolution over three TSRs. In the first subsection, the simulated and experimental flowfield is discussed in detail. Contours of vorticity are used to visualise the near-blade wake, (with the same contour levels maintained for all images). Following this, the performance of the turbine is analysed in relation to the flow field aerodynamics of both the simulation and experimental measurement. Differences between the experimental and computational $\mathbf{C_p}$ are also explained.

It should be noted that this paper details significant new results which build upon the only comparable previous study by Ferreira et al. [12] in which the flow field development around an entire rotor blade revolution is discussed at a small number of selected locations in [12]. Differences are expected due to the different solidity and profile the current study uses the NACA0022, whereas [12] uses the NACA015. The overall blockage between the studies is very close; currently 29% and 32% in [8].

## 3.1 Correlation of Experimental and Simulated Flowfields

The geometrically derived value of $\boldsymbol{\alpha}$ becomes increasingly erroneous as $\boldsymbol{\lambda}$ increases due to the greater impedance which is presented to the flow by the rotor. The rotor exerts a force on the incoming flow, slowing it down and forcing the streamtube to expand around the turbine, in order to conserve mass flow rate. To account for this, the discussion of the flow physics are discussed relative to a corrected angle of attack, $\boldsymbol{\alpha_c}$, which has been obtained from the CFD solution via the method detailed in [3]. For comparison and completeness, the geometrically derived value is also presented.

### 3.1.1 Flowfield Analysis, λ = 2

At the λ = 2 condition, the experimental PIV visualisations shows the onset of stall occurring around **ψ** = 60° (Figure 13a), with the first leading-edge vortex leaving the surface at **ψ** = 70° where roll-up at the trailing edge is also shown (Figure 13b). The CFD simulation shows a similar process with a very small lag behind the experiment (Figures 12f and 12g). Figure 12 shows $\boldsymbol{\alpha_c}$ = 17.3° at **ψ** = 60°, which is certainly above the static-stall angle. The rapid increase in $\boldsymbol{\alpha_c}$ can be thought of as a 'pitch-up' motion; in tests on a pitching aerofoil such a motion is shown to increase the angle of attack at which stall occurs [8]. The simulation shows the stall process originating from a gradual trailing edge separation; this differs from the experiment which appears to show a more sudden separation at the leading edge. The vortex shedding between **ψ** = 80°, and **ψ** = 100°, is also similar between the experiment (Figures 13c to 13e) and the simulation (Figures 13h to 13j), with the simulation continuing to lag very slightly behind the experimental flowfield.

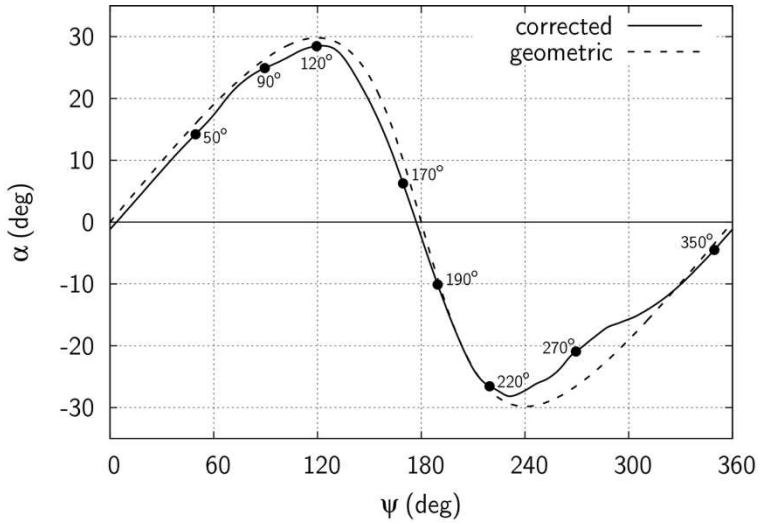


Figure 12. A plot of $\alpha$ vs $\psi$ for $\lambda$ = 2, with key positions in the rotation indicated.

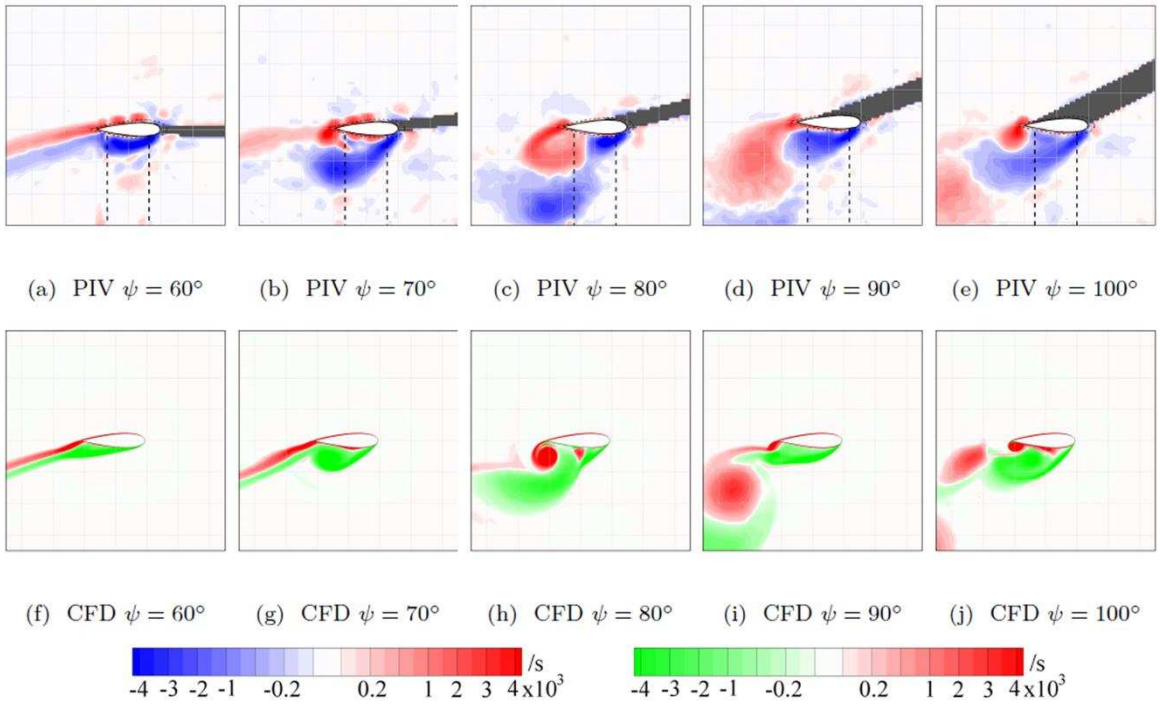


Figure 13. Plots of vorticity showing the onset of stall, as shown by the PIV measurements and as predicted using the CFD model for $\lambda = 2$

Towards the mid-rotation point ($\psi$ = 180°), both the sets of data show a significant delay in the flow reattachment as the angle of attack rapidly decreases. The simulation shows quite a sudden change from the shedding of large structures to a much smaller wake (Figures 14f to 14h), whereas the PIV visualisations reveal this to be a more gradual process in the experiment (Figures 14a to 14c). Either way, this process is likely to keep the performance of the rotor blade lower than would be the case with a more rapid re-attachment of the flow. Despite $\alpha_c$ dropping to 5.9°, the flow has not yet attached by $\psi$ = 170°. As with the experiment, the reattachment of the flow is shown to occur at around $\psi$ = 190°, where $\alpha_c$ = −10.5°. Shortly after this, the flow is shown to stall in the early stages of the downwind part of the rotation. At $\psi$ = 230°, where $\alpha_c$ has already reached −26.7° (Figure 12), the CFD simulation shows the flow to be detached (Figure 14i), as did the PIV measurements (Figure 14d). The shedding process is also shown to progress at similar rate between the CFD (Figure 14j) and PIV visualisations (Figure 14e). The rapid decrease in $\alpha$ can be thought of as a 'pitch-down' motion; in tests on a pitching aerofoil such a motion is shown to lead to a delayed reattachment of the flow as part of the dynamic stall process, which results in significant hysteresis in the aerodynamic forces [8]. As the angle of attack reduces

significantly from $\psi$ = 260° onwards (Figure 12), the CFD shows a gradually reducing depth of stall with the shed vortices also gradually reducing in size (Figures 15f to 15i), which matches the PIV measurements well (Figures 15a to 145).

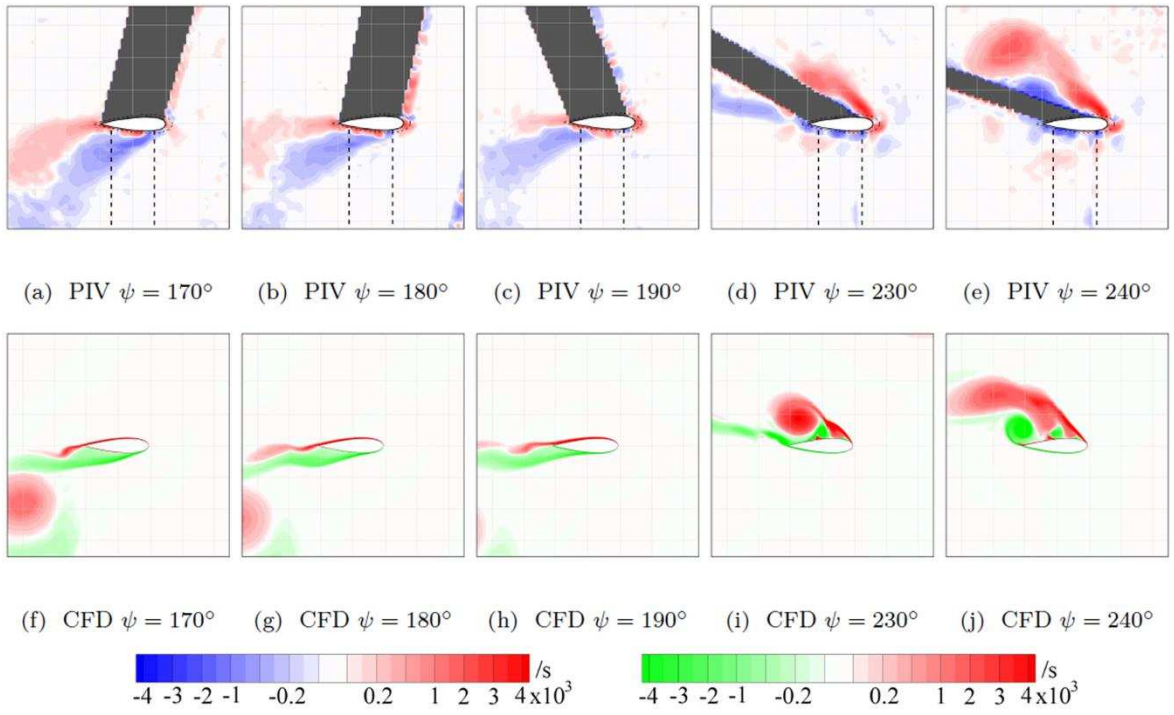


Figure 14. Plots of vorticity showing the mid-rotation reattachment process and downwind stall, as shown by the PIV measurements and as predicted using the CFD model for $\lambda$ = 2

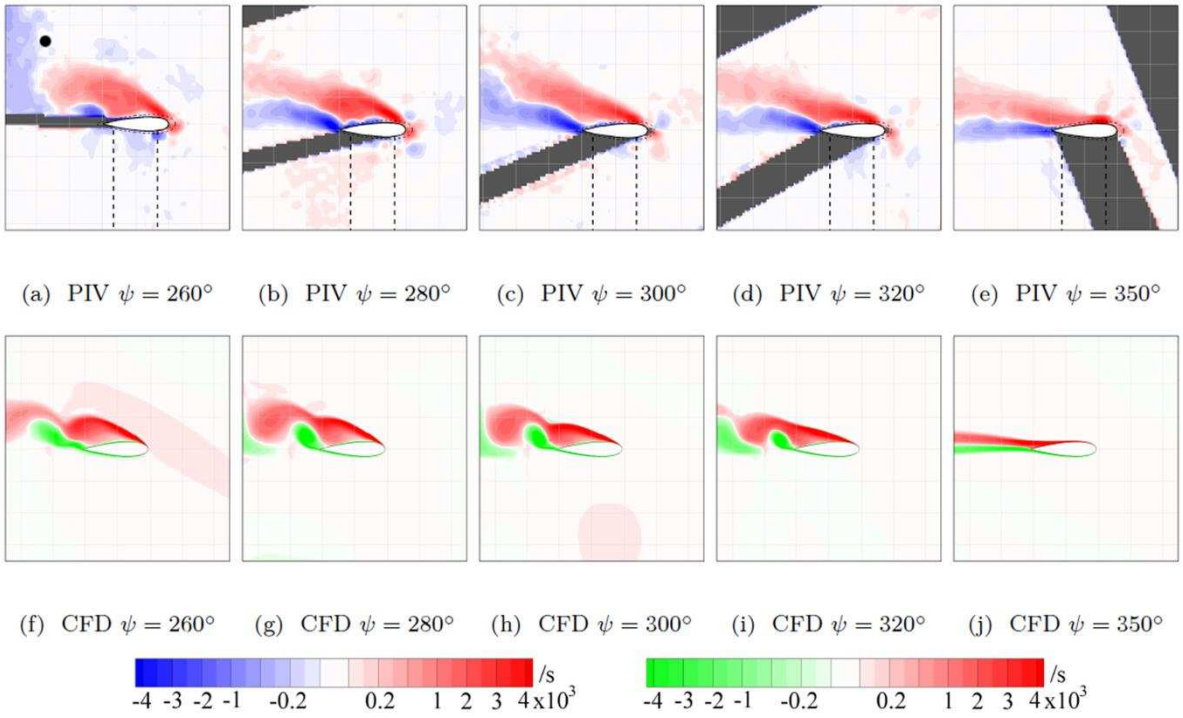

Figure 15. Plots of vorticity showing the downwind post-stall vortex shedding and eventual reattachment, as shown by the PIV measurements and as predicted using the CFD model for $\lambda = 2$

Understandably, the experimental flowfield varies in this region between rotations and so the individual vortex positions cannot be matched to the simulation due to the ensemble averaging of the 100 instantaneous experimental measurements. As a result there is some smearing of the experimental data. The simulation shows reattachment occurring before $\psi = 350°$ (Figure 15j), which is in advance of the experimental flow field (Figure 15e). This would result in lower drag being predicted for this part of the rotation. Averaged around an entire rotation the performance coefficient is very similar between the experiments and CFD (Figure 22)

*Summary of Simulated Flowfield at $\lambda = 2$*

The CFD-simulated flowfield and the PIV visualisations have been shown to be very well-matched for $\lambda = 2$. The position that the flow detaches from the blade surface is closely matched for both upwind and downwind parts of the rotation, with only a small delay ($<< 10°$ in $\psi$) being observed for the upwind part. However, the onset of stall appears to be different between the experiment and simulation, with the simulation showing a gradual separation progressing forwards from the trailing edge, while the experiment shows a more sudden leading edge roll-up. The shedding behaviour is also well-matched, with similar scales of vortices being shed at a similar rate. The most significant CFD-PIV differences are observed in predicting reattachment: small differences between the experiment and simulation are observed in the first reattachment at the mid-rotation; however, the simulation predicts the second reattachment to occur at least 10° in $\psi$ earlier in the rotation when compared to the experiment.

### 3.1.2 Flowfield Analysis, $\lambda = 3$

At $\lambda = 3$, the experimental PIV measurements show the onset of separation and subsequent leading-edge vortex roll-up occurring between $\psi = 80°$ and 90° (Figures 17a and 17b). At the onset of stall $\alpha_c = 15.2°$ (Figure 16), which is slightly lower than for $\lambda = 2$ condition; a drop in the rate of change of angle of attack would be expected to reduce the dynamic stall angle. Relative to the experiment, the CFD simulation (Figures 17f and 17h) again show a delay in the stalling process: the roll up of the first vortex is delayed by an approximate 10° difference

in ψ, which will result in incorrect lift and drag predictions for this region. Again, the simulation shows stall beginning with a gradual separation from the trailing edge. The post-stall vortex shedding is show in the experiments (Figures 17c to 17e) and simulations (Figures 17h to 17j), with a similar vortex shedding rate observed, and similar reduction in the depth of stall shown as the angle of attack reduces in this region of the rotation (Figure 16). The 10° in ψ phase difference is maintained for the measurements shown in Figure 17.

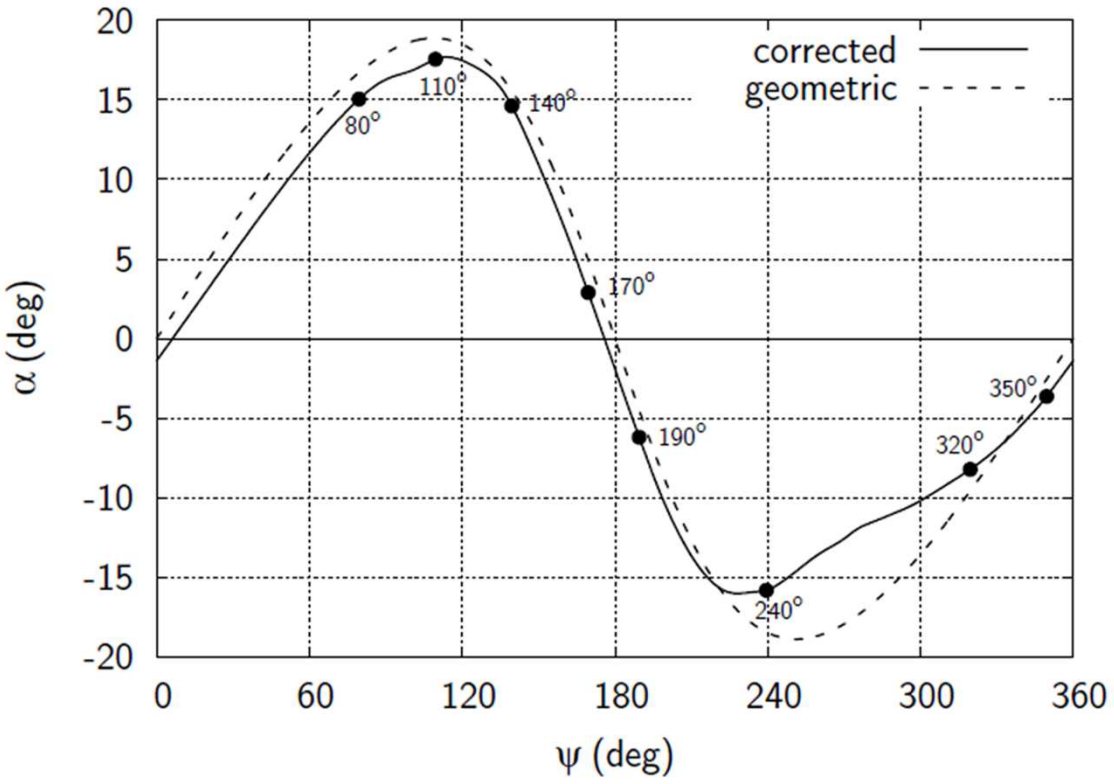


Figure 16. A plot of $\alpha$ vs $\psi$ for $\lambda = 3$, with key positions in the rotation indicated.

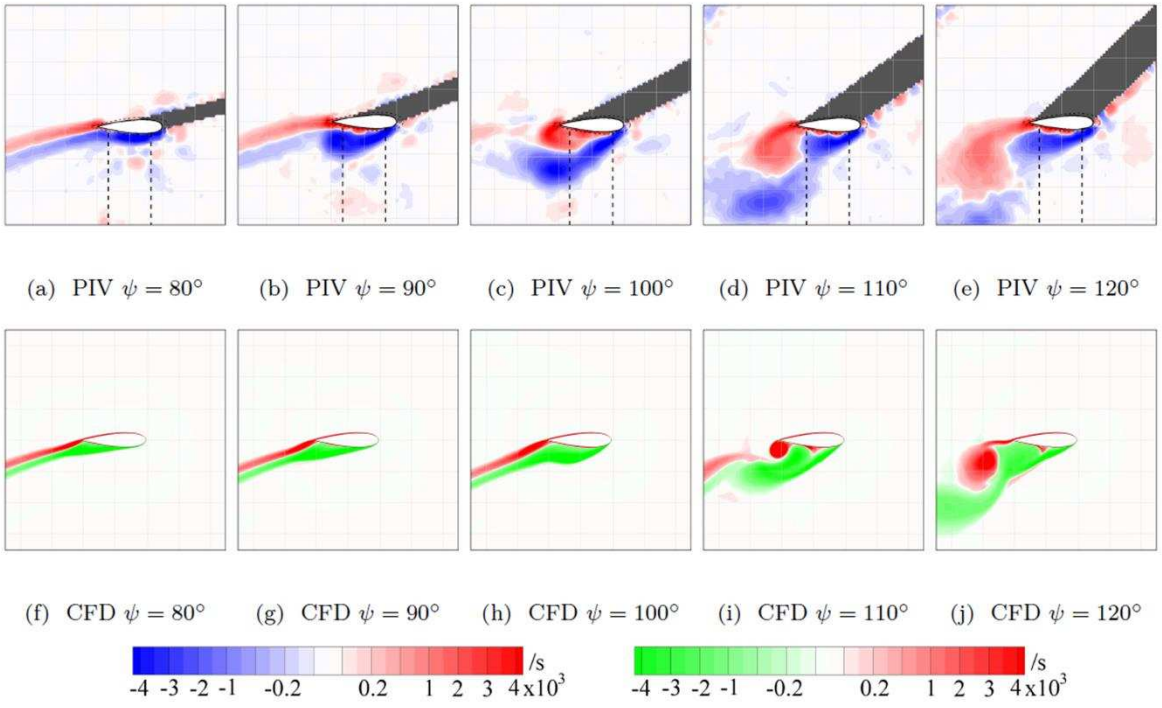


Figure 17. Plots of vorticity showing the onset of stall and post-stall vortex shedding, as shown by the PIV measurements and as predicted using the CFD model for $\lambda = 3$

As for the $\boldsymbol{\lambda} = 2$ condition, the reattachment prediction at $\boldsymbol{\lambda} = 3$ is reasonably well-matched between the experiment (Figures 18a to 18e) and simulation (Figures 18f to 18j). The gradual reduction in the scale of the shed vortices also appears to be well-matched. Vortices shed by the upstream blade are visible in the CFD-predicted flowfield at $\boldsymbol{\psi} = 190°$ (Figure 18j); some trace amounts vorticity of matching sign can also be seen in the equivalent experimental plot (Figure 18e) but the dissipation and collapse of the vortex structure in the experiment clearly happens at a faster rate, as would be expected versus a two-dimensional simulation.

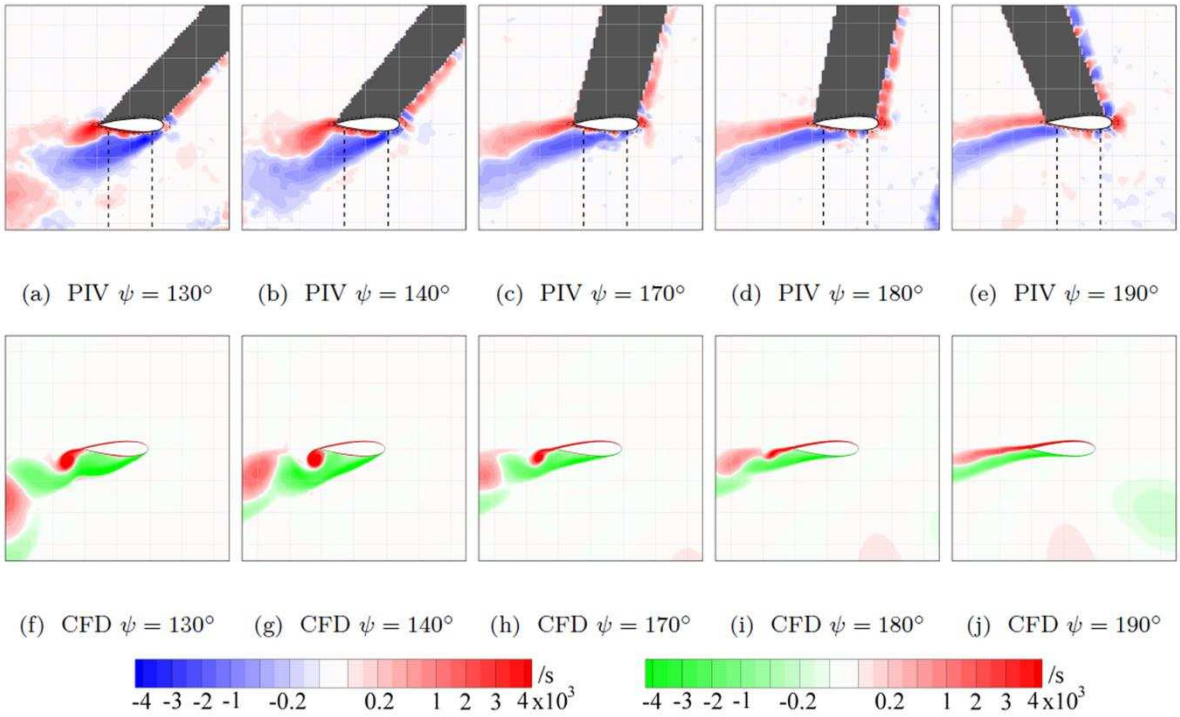


Figure 18. Plots of vorticity showing the post-stall flow recovery and mid-rotation reattachment process, as shown by the PIV measurements and as predicted using the CFD model for $\lambda = 3$

Although $\boldsymbol{\alpha_c}$ reaches a maximum of 16° at $\boldsymbol{\psi}$ = 228°, the simulation predicts the onset of stall in the downwind portion of the rotation to occur around $\boldsymbol{\psi}$ = 240° (Figure 19f), as do the PIV measurements (Figure 19a); however, the experimentally observed thicker wake (relative to attached flow at other positions) indicates partially-separated flow. The extent of the wake shown in the experiment at $\boldsymbol{\psi}$ = 250° (Figure 19b) further suggests that full reattachment does not occur around the mid-rotation point. The simulation differs (Figure 19g), instead showing a sudden separation to stall from a fully-attached condition, as was observed in the upwind part of the rotation (around $\boldsymbol{\psi}$ = 90°). As the angle of attack reduces significantly beyond $\boldsymbol{\psi}$ = 270° (Figure 16), the simulation shows a gradually reducing depth of stall with the shed vortices also gradually reducing in size (Figures 19h to 19j), which matches the experimental measurements well (Figures 19c to 19e). The reattachment of the flow in the simulation again precedes that which is shown by PIV in the experiment by around 20° in $\boldsymbol{\psi}$.

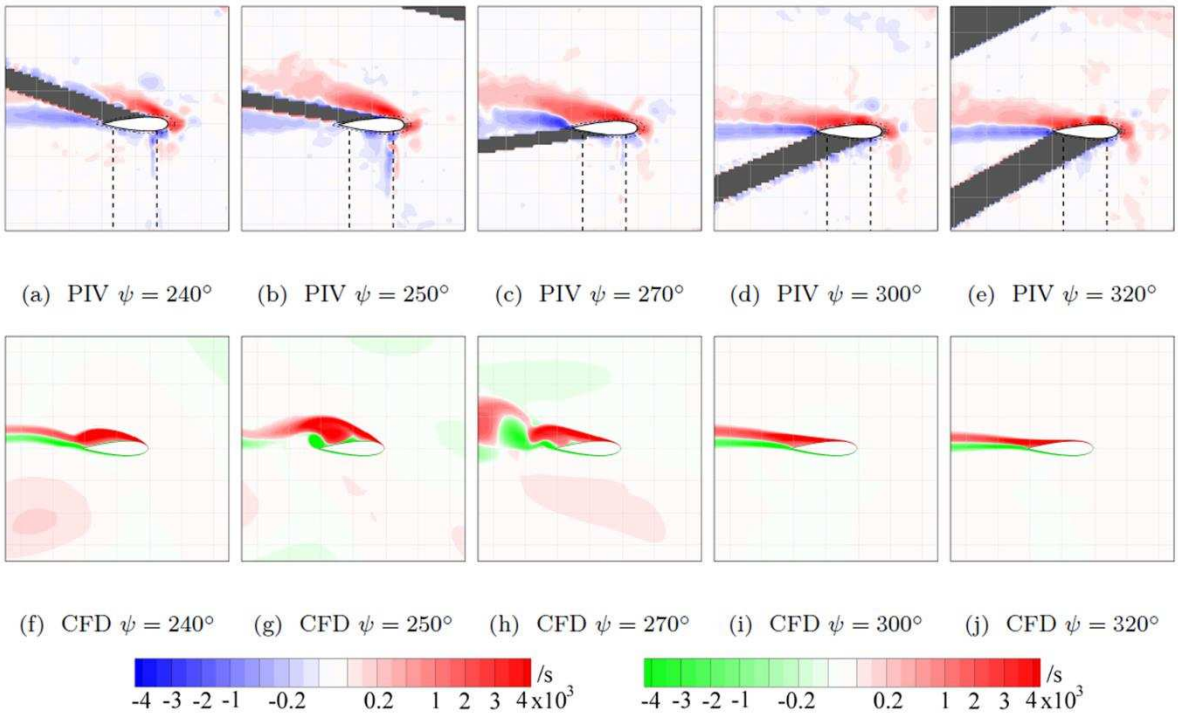


Figure 19. Plots of vorticity showing the downwind onset of stall, vortex shedding, and eventual reattachment as shown by the PIV measurements and as predicted using the CFD model for $\lambda = 3$

Summary of Simulated Flowfield at $\boldsymbol{\lambda} = 3$

For the $\boldsymbol{\lambda} = 3$ condition, the position that the flow detaches from the blade surface is slightly delayed, more so than for the $\boldsymbol{\lambda} = 2$ condition, in both the upwind and downwind parts of the rotation. The shedding behaviour is again well-matched between CFD and PIV, with similar scales of vortices being shed at a similar rate. The most significant CFD-PIV differences are once again observed in predicting the reattachment process: only small differences are observed in the first reattachment at the mid-rotation point, a much earlier second reattachment is observed in the downwind part of the rotation, with the simulation showing earlier reattachment by around 20° in $\boldsymbol{\psi}$**.** With a slightly delayed stall and earlier reattachment, the simulation is likely to over predict the performance measured in the experiment, this is indeed the case as shown later in Section 3.2.

### 3.1.3 Flowfield Analysis, $\boldsymbol{\lambda} = 4$

At this condition, the turbine is generating power so more attached flow is likely to be seen in both the simulations and experimental data. Later detachment of the flow is seen now, from between $\boldsymbol{\psi}$ = 110° and $\boldsymbol{\psi}$ = 120° where the CFD simulation shows a gradual detachment moving forward from the trailing edge (Figures 21f and 21g), which is similar to that in the

experiment (Figures 21a and 21b). However, as the angle of attack reduces beyond as the rotor reaches $\psi$ = 130°, the simulation (Figures 21h and 21i) does not show the same vortex shedding as is shown in the experimental flowfield observations (Figures 21c and 21d). Figure 20 shows that $\alpha_c$ has already peaked $\psi$ = 105° however, at $\psi$ = 130° $\alpha_c$ is beginning to drop rapidly and, in the experiment, a large vortex rolls up in the already separated flow as the 'pitch-down' motion occurs. In the experiment, the stalled flow eventually reattaches around $\psi$ = 180° (Figure 21e), but no large separation is shown in the CFD and the separation point simply retreats back toward the trailing edge as the angle of attack reduces (Figures 21d to 21e). As a result, the simulated drag between $\psi$ = 130° and 180° will be significantly higher than the experimental case, and the lift significantly lower. This is shown in the performance results at this TSR (see Figure 22) although the performance difference is also due to 3 dimensional effects not present in the CFD. Due to the significantly reduced relative velocity in the downwind part of the rotation, the range in $\alpha$ is greatly reduced (Figure 20), and attached flow is shown for all of the downwind part of the rotation.

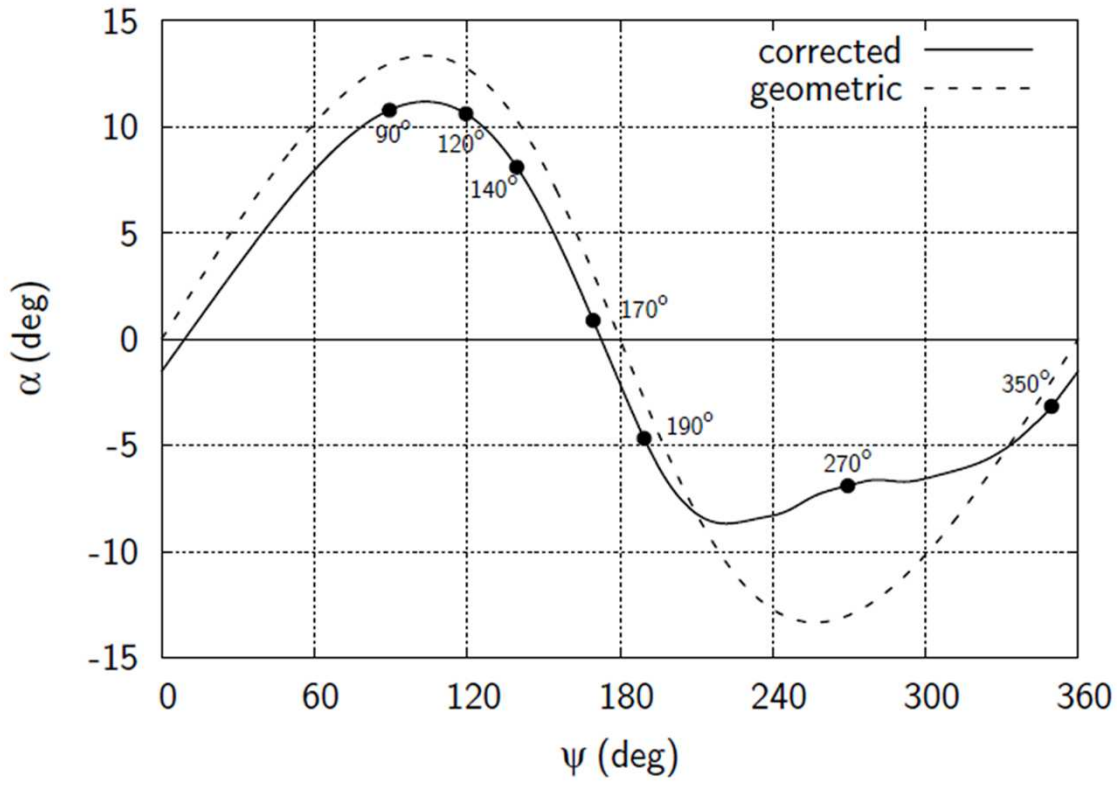


Figure 20. A plot of $\alpha$ vs $\psi$ for $\lambda$ = 4, with key positions in the rotation indicated.

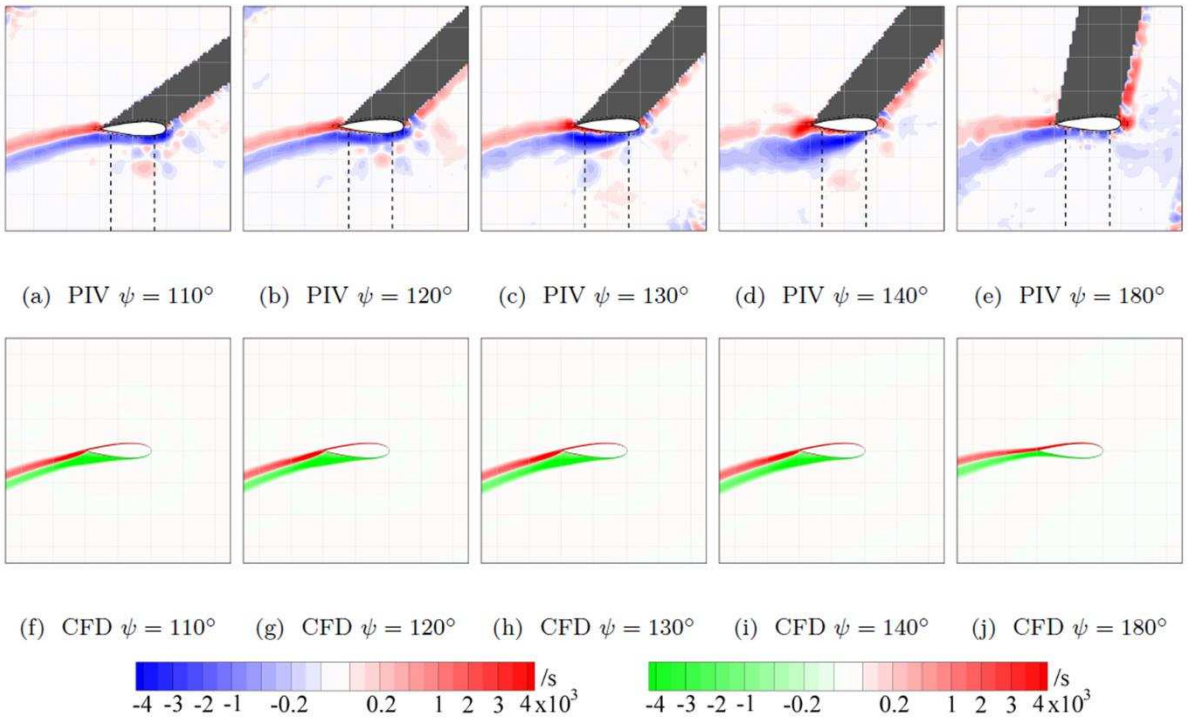


Figure 21. Plots of vorticity showing the onset of stall, brief vortex shedding, and subsequent flow recovery as shown by the PIV measurements and as predicted using the CFD model for $\lambda = 4$

Summary of Simulated Flowfield at $\lambda = 4$

The lack of a flow separation in the latter stages of the upwind part of the rotation is the only main point to note when comparing the flowfields of the simulation and experiment for the $\boldsymbol{\lambda}$ = 4 condition. The performance in this region of the rotation would certainly be very different between the CFD simulation and the experiment, with the simulation very likely to be predicting lower drag and higher lift than would be actually be experienced by the blade in the wind tunnel experiment. For the rest of the rotation, the flow is attached in both the simulation and experiment due to the lowered angle of attack.

## 3.2 Linking Experimental and Simulated Performance

Comparison of the CFD-simulated flowfield with the experimental observations by PIV has revealed a good match between the two, showing that it is possible to simulate the basic VAWT blade flow physics, which includes dynamic stall and reattachment. A good representation of the general flow physics is an important step towards a useful CFD VAWT model; however, a correct $\mathbf{C_p}$ prediction is likely to be the ultimate goal for most future studies. With this in mind, a comparison of the CFD-predicted $\mathbf{C_p}$ - $\boldsymbol{\lambda}$ relationship with the

experiment is made by adding $\mathbf{C_p}$ values from additional simulations to map-out the full curve.

Results of the CFD-predicted performance are shown alongside the experimental measurements in Figure 22. The first, and most obvious observation is that the maximum $\mathbf{C_p}$ is over-predicted in the simulation by a significant margin, but this is expected as the 2D simulation does not include all of the losses that exist in the experiment (which is of course 3D) such as those due to blade tip effects and the interaction between the blades and the supporting structure. The simulation predicts $\mathbf{C_{p-max}}$=0.36, whereas the experiment has measured $\mathbf{C_{p-max}}$ = 0.14, clearly the predicted blade forces are quite different between the two cases. However, it should be noted that from the perspective of this study the shape curve shape is well represented and that is most important: from $\boldsymbol{\lambda}$ = 1 the $\mathbf{C_p}$ drops to form a negative trough in the performance curve just above $\boldsymbol{\lambda}$ = 2, and from here performance rapidly improves with increasing $\boldsymbol{\lambda}$ with both CFD and experiment crossing to positive $C_p$ at similar $\boldsymbol{\lambda}$ until a maximum $\mathbf{C_p}$ is encountered in both cases at around $\boldsymbol{\lambda}$ = 4 after which, with further increases in $\boldsymbol{\lambda}$, a steep drop in performance in experienced.

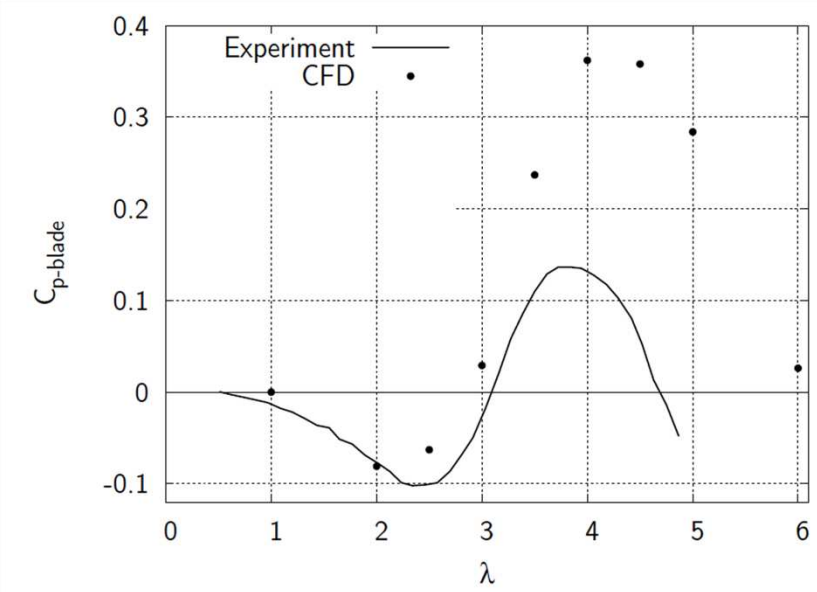


Figure 22. Cp−blade vs λ as predicted by the CFD simulation and as measured in the experiment

The simulated $\mathbf{C_p}$ matches the experiment closely for low tip speed ratios, and the flowfield has previously been shown to compare well compared for $\boldsymbol{\lambda}$ = 2. However, the differences in the $\mathbf{C_p}$ between CFD and experiment become more and more significant as $\boldsymbol{\lambda}$ is

increased. Increased stall delay and earlier flow reattachment were observed at $\lambda$ =3, and understandably the CFD predicts higher $\mathbf{C_p}$ at this tip speed ratio. Most significantly, no separation at all was predicted for $\lambda$ =4, which would be expected to lead to a significant over-estimation of $\mathbf{C_p}$ at this condition. Certainly, some differences are expected due to 3D effects: a similar comparison between experiment and 2D CFD has been shown by [7], whose blades had a similar aspect ratio of 17. Further to this, [18] show a much improved match between experimental results and their 3D CFD simulations while the equivalent 2D CFD results were shown to give substantial over-prediction. However, the model turbine used by Howell et al. had a very low aspect ratio of 4 (in this study it is 15), and so the substantial 2D CFD versus 3D CFD differences are not surprising. Induced drag effects increase with the square of lift, and so the wing-tip effect would be expected to become more significant as the blade reaches an optimum $\lambda$ and the blade spends more of the rotation at a high-lifting condition. Results obtained by [23] have shown an increased effect of aspect ratio with $\lambda$, with a change in aspect ratio AR from 160 to 15 leading to an approximate $\mathbf{C_p}$ drop of 1/3 at $\lambda$ = 5 and only 1/5 at $\lambda$ = 3. This may, in part, account for why the flowfield visualisations match-up reasonably well, yet the $\mathbf{C_p}$ prediction does not. Further to this, a poor prediction of zero-lift drag, which has the most influence at high $\lambda$ [23] where the range in $\alpha$ is lowest, may also be the cause of differences. Additional investigations would be required to better evaluate the model's ability to correctly predict the viscous drag, the contribution of which is most significant at low angle of attack.

# 4 Conclusion

The comparison of the CFD-simulated and experimental flowfields have shown a good match at the three different tip speed ratios tested. The basic process of attached flow, stall, vortex shedding and reattachment is shown for the $\lambda$ = 2 and 3 conditions, although the brief stall at $\lambda$ = 4 is missing in the simulations. A small delay in detachment and earlier reattachment is shown in the simulation, indicating that the CFD-simulated flow is generally more inclined to be attached to the blade surface.

Significant differences between simulated and experimental $\mathbf{C_p}$ is noted at higher $\lambda$. However, in general, the performance curve is well-formed, with the same basic trends observed with changing $\lambda$ (albeit they are scaled by larger amounts) and the gradients in the curve at each of these points are very similar. This all suggests that similar fundamental changes in the flow physics are contributing to the change in curve shape at each condition in

both the simulation and the experimental case. Further work is required to assess the impact of three-dimensional effects on VAWT performance, particularly at higher tip speed ratios, this being crucial to correct prediction if aiming to realise any real-word device.

Based on the results and analysis in this study, the continued use of the CFD model is well-justified, particularly where supplemented with experimental data for validation.

**Acknowledgements**

The authors would like to thank the workshop technicians at the Department of Mechanical Engineering for the manufacture of the turbine and all the associated measurement subsystems. For funding this research, Jonathan Edwards would like to thank the University of Sheffield Studentship Program and Louis Danao would like to thank the Engineering Research and Development for Technology Program of the Department of Science and Technology through the University of the Philippines' College of Engineering.

## References

[1] Iida, A., Mizuno, A., and Fukudome, K., 2007, "Numerical Simulation of Unsteady Flow and Aerodynamic Performance of Vertical Axis Wind Turbines with LES," 16th Australasian Fluid Mechanics Conference, Gold Coast, Australia, pp.1295-1298.

[2] Mertens, S., Van Kuik, G., and Van Brussel, G. J. W., 2003, "Performance of a High Tip Speed Ratio H-Darrieus in the Skewed Flow on a Roof," 41st AIAA Aerospace Sciences Meeting and Exhibit, Reno, Nevada, USA. AIAA-2003-0523.

[3] Edwards, J. M., Danao, L. A., and Howell, R., 2012, "Novel Experimental Power Curve Determination and Computational Methods for the Performance Analysis of Vertical Axis Wind Turbines," Journal of Solar Energy Engineering, Volume 134, Issue 3, 2012.

[4] C J Simao Ferreira, C. J., van Brussel, G. J. W., and van Kuik, G., 2008, "2D CFD Simulation of Dynamic Stall on a Vertical Axis Wind Turbine: Verification and Validation with PIV Measurements" 45th AIAA Aerospace Sciences Meeting and Exhibit, Reno, Nevada, USA.

[5] Tullis, S., Fiedler, A., McLaren, K., and Ziada, S., 2008, “Medium-Solidity Vertical Axis Wind Turbines for use in Urban Environments” 7th World Wind Energy Conference, Kingston, Ontario, Canada.

[6] Raciti Castelli, M., Englaro, A., and E Benini, E., 2011, “The Darrieus Wind Turbine: Proposal for a New Performance Prediction Model Based on CFD” Energy, 36(8):4919-4934.

[7] Wang, S. Hughes, K.J., Ingham, D.B., Ma, L.a, , Pourkashanian, M. and Tao, Z. Edwards, J.M., Howell, R.J., Danao, L.A.M., Sobotta, D., Qin N. “An experimental investigation into the aerodynamics of a vertical axis wind turbine using PIV” Under review with the Journal of Wind Energy and Industrial Aerodynamics.

[8] Lee, T., and Gerontakos, P., 2004, “Investigation of Flow over an Oscillating Airfoil”, Journal of Fluid Mechanics, 512:313-341.

[9] Mccroskey, W. J., 1981, "The Phenomenon of Dynamic Stall," Technical Report No. NASA TM-81264, Ames Research Center, Moffett Field, California.

[10] Mclaren, K., Tullis, S., and Ziada, S., 2011, "Computational Fluid Dynamics Simulation of the Aerodynamics of a High Solidity, Small-Scale Vertical Axis Wind Turbine," Wind Energy, 15(3), pp. 349-361.

[11] Wang, S., Ingham, D. B., Ma, L., Pourkashanian, M., and Tao, Z., 2010, "Numerical Investigations on Dynamic Stall of Low Reynolds Number Flow around Oscillating Airfoils," Computers and Fluids, 39(9), pp. 1529-1541.

[12] Simao Ferreira, C. J., Van Kuik, G., Van Brussel, G. J. W., and Scarano, F., 2009, “Visualization by PIV of Dynamic Stall on a Vertical Axis Wind Turbine,” Experiments in Fluids, 46(1), pp. 97-108.

[13] N Fujisawa and SShibuya. Observations of Dynamic Stall on Darrieus Wind Turbine Blades. Journal of Wind Engineering and Industrial Aerodynamics, 89(2001):201-214, 2000.

[14] Yen, J. , Ahmed, N.A., “Enhancing vertical axis wind turbine by dynamic stall control using synthetic jets”, Journal of Wind Engineering and Industrial Aerodynamics, Volume 114, March 2013, Pages 12-17

[15] Greenblatt, D., Ben-Harav, A., Schulman, M., “Dynamic stall control on a vertical axis wind turbine using plasma actuators ( Conference Paper ) “ 50th AIAA Aerospace Sciences Meeting Including the New Horizons Forum and Aerospace Exposition, 2012, Article number AIAA 2012-0233

[16] J. H. Strickland, B. T. Webster and T. Nguyen. A Vortex Model of the Darrieus Turbine: An Analytical and Experimental Study. J. Fluids Eng. 101(4), 500-505 (Dec 01, 1979).

[17] Van Bussel, G. J. W., Polinder, H., and Sidler, H. F. A., 2004, "The Development of Turby, a Small Vawt for the Built Environment," Global Windpower 2004 Conference and Exhibition, Chicago, IL, USA, pp. 10.

[18] Penna, P., and Bertenyi, T., 2008, "Full-Scale Wind Tunnel Testing of the QR5 Vertical Axis Wind Turbine," 46th AIAA Aerospaces Sciences Meeting and Exhibit, Reno, Nevada, USA.

[19] Howell, R., Qin, N., Edwards, J., and Durrani, N., 2010, "Wind Tunnel and Numerical Study of a Small Vertical Axis Wind Turbine," Renewable Energy, 35(2), pp. 412-422.

[19] Edwards, J. E., "The Influence of Aerodynamic Stall on the Performance of Vertical Axis Wind Turbines", PhD thesis, Department of Mechanical Engineering, University of Sheffield.

[21] ANSYS Inc. Fluent 12.1 user guide and manual. Released 01/10/2009.

[22] Hamada K, Smith TC, Durrani N, Qin N, Howell R. Unsteady Flow Simulation and Dynamic Stall Around Vertical Axis Wind Turbine Blades. 46th AIAA Aerospaces Sciences Meeting and Exhibit. Reno, Nevada, USA 2008.

[23] McIntosh, S. C., 2009, "Wind Energy for the Built Environment" PhD thesis, Department of Engineering, Trinity Hall, Cambridge.